

# *In vivo* high-resolution video-rate spectral-domain optical coherence tomography of the human retina and optic nerve

N. A. Nassif, B. Cense, B. H. Park, M. C. Pierce, S. H. Yun, B. E. Bouma, G. J. Tearney

Harvard Medical School & Wellman Center for Photomedicine, Massachusetts General Hospital  
50 Blossom Street, BAR 724, Boston MA 02114

T. C. Chen

Massachusetts Eye and Ear Infirmary and Harvard Medical School,  
243 Charles Street, Boston, Massachusetts 02114

J. F. de Boer

Harvard Medical School & Wellman Center for Photomedicine, Massachusetts General Hospital  
50 Blossom Street, BAR 724, Boston MA 02114

[deboer@helix.mgh.harvard.edu](mailto:deboer@helix.mgh.harvard.edu)

**Abstract:** An ultra-high-speed spectral-domain optical coherence tomography system (SD-OCT) was developed for imaging the human retina and optic nerve *in vivo* at a sustained depth profile (A-line) acquisition speed of 29 kHz. The axial resolution was 6  $\mu\text{m}$  in tissue and the system had shot-noise-limited performance with a maximum sensitivity of 98.4 dB. 3-dimensional data sets were collected in 11 and 13 seconds for the macula and optic nerve head respectively and are presented to demonstrate the potential clinical applications of SD-OCT in ophthalmology. Additionally, a 3-D volume of the optic nerve head was constructed from the acquired data and the retinal vascular network was visualized.

©2004 Optical Society of America

**OCIS codes:** (170.4470) Ophthalmology; (170.3890) Medical optics instrumentation; (110.6880) Three-dimensional image acquisition; (110.4280) Noise in imaging systems; (030.4280) Noise in imaging systems.

---

## References and Links

1. D. Huang, E. A. Swanson, C. P. Lin, J. S. Schuman, W. G. Stinson, W. Chang, M. R. Hee, T. Flotte, K. Gregory, C. A. Puliafito, "Optical coherence tomography," *Science* **254**, 1178-1181 (1991).
2. A. F. Fercher, C. K. Hitzenberger, G. Kamp, S. Y. Elzaiat, "Measurement of intraocular distances by backscattering spectral interferometry," *Opt. Commun.* **117**, 43-48 (1995).
3. G. Hausler, M. W. Lindner, "Coherence radar and spectral radar - new tools for dermatological diagnosis," *J. Biomed. Opt.* **3**, 21-31 (1998).
4. A. F. Fercher, W. Drexler, C. K. Hitzenberger, T. Lasser, "Optical coherence tomography - principles and applications," *Reports on Progress in Physics* **66**, 239-303 (2003).
5. R. Leitgeb, C. K. Hitzenberger, A. F. Fercher, "Performance of fourier domain vs. Time domain optical coherence tomography," *Opt. Express* **11**, 889-894 (2003), <http://www.opticsexpress.org/abstract.cfm?URI=OPEX-11-8-889>
6. J. F. de Boer, B. Cense, B. H. Park, M. C. Pierce, G. J. Tearney, B. E. Bouma, "Signal to noise gain of spectral domain over time domain optical coherence tomography," *Opt. Lett.* **28**, 2067-2069 (2003).
7. M. A. Choma, M. V. Sarunic, C. Yang, J. A. Izatt, "Sensitivity advantage of swept source and fourier domain optical coherence tomography," *Opt. Express* **11**, 2183-2189 (2003), <http://www.opticsexpress.org/abstract.cfm?URI=OPEX-11-18-2183>
8. N. Nassif, B. Cense, B. H. Park, S. H. Yun, T. C. Chen, B. E. Bouma, G. J. Tearney, J. F. de Boer, "In-vivo human retinal imaging by ultra high-speed spectral domain optical coherence tomography," *Opt. Lett.* **29**, (2004) (to be published).

9. Drexler W, Sattmann H, Hermann B, Ko TH, Stur M, Unterhuber A, Scholda C, Findl O, Wirtitsch M, Fujimoto JG, F. AF., "Enhanced visualization of macular pathology with the use of ultrahigh-resolution optical coherence tomography," *Archives of Ophthalmology* **121**, 695-706 (2003).
10. American National Standards Institute, *American national standard for safe use of lasers z136.1* (American National Standards Institute, Orlando, 2000).
11. M. Wojtkowski, R. Leitgeb, A. Kowalczyk, T. Bajraszewski, A. F. Fercher, "In vivo human retinal imaging by fourier domain optical coherence tomography," *J. Biomed. Opt.* **7**, 457-463 (2002).
12. M. Wojtkowski, T. Bajraszewski, P. Targowski, A. Kowalczyk, "Real-time in vivo imaging by high-speed spectral optical coherence tomography," *Opt. Lett.* **28**, 1745-1747 (2003).
13. R. Leitgeb, L. Schmetterer, W. Drexler, A. Fercher, "Real-time assessment of retinal blood flow with ultrafast acquisition by color doppler fourier domain optical coherence tomography," *Opt. Express* **11**, 3116-3121 (2003), <http://www.opticsexpress.org/abstract.cfm?URI=OPEX-11-23-3116>
14. B. Cense, T. C. Chen, B. H. Park, M. C. Pierce, J. F. de Boer, "In vivo depth-resolved birefringence measurements of the human retinal nerve fiber layer by polarization-sensitive optical coherence tomography," *Opt. Lett.* **27**, 1610-1612 (2002).
15. F. W. Campbell, D. G. Green, "Optical and retinal factors affecting visual resolution," *J. Physiol. (London)* **181**, 576-593 (1965).
16. B. H. Park, M. C. Pierce, B. Cense, J. F. de Boer, "Real-time multi-functional optical coherence tomography," *Opt. Express* **11**, 782-793 (2003), <http://www.opticsexpress.org/abstract.cfm?URI=OPEX-11-7-782>
17. C. Dorrer, N. Belabas, J. Likforman, M. Joffre, "Spectral resolution and sampling issues in fourier transform spectral interferometry," *Journal of the Optical Society of America B* **17**, 1795-1802 (2000).
18. S. H. Yun, G. J. Tearney, B. E. Bouma, B. H. Park, J. F. de Boer, "High-speed spectral-domain optical coherence tomography at 1.3  $\mu\text{m}$  wavelength," *Opt. Express* **11**, 3598-3604 (2003), <http://www.opticsexpress.org/abstract.cfm?URI=OPEX-11-26-3598>
19. B. R. White, M. C. Pierce, N. Nassif, B. Cense, B. H. Park, G. J. Tearney, B. E. Bouma, T. C. Chen, J. F. de Boer, "In vivo dynamic human retinal blood flow imaging using ultra-high speed spectral domain optical doppler tomography," *Opt. Express* **11**, 3490-3497 (2003), <http://www.opticsexpress.org/abstract.cfm?URI=OPEX-11-25-3490>

## 1. Introduction

Optical coherence tomography (OCT) is an interferometric imaging technique that allows for high-resolution, cross-sectional imaging of biological tissue [1]. In the standard time-domain (TD) implementation of OCT, the position of the reference mirror in the interferometer is rapidly scanned in order to obtain a depth profile (A-line) within a sample. An alternative method of retrieving depth information examines the cross-spectral density to reconstruct the interferogram by detecting the interference signal as a function of wavelength [2-4]. Spectral-domain optical coherence tomography (SD-OCT), also known as Fourier-domain OCT (FD-OCT), does not require modulation of the reference arm length and therefore has potential for faster image acquisition rates. Although this method has long been proposed and demonstrated, only recently have there been efforts to explicitly show that SD-OCT can produce a better detection sensitivity than the time domain method [5-7]. Recent work has experimentally demonstrated a 148-fold (21.7 dB) sensitivity improvement with SD-OCT [8].

TD-OCT has been applied extensively in ophthalmology, where cross-sectional OCT images of the retina have provided useful information regarding the presence or progression of specific ocular diseases [9]. The acquisition rate of current clinical and pre-clinical TD-OCT systems is limited by sensitivity and the maximum permissible incident power on the eye [10], preventing comprehensive screening of large retinal areas. The sensitivity improvement of SD-OCT allows for dramatically increased acquisition speeds without compromising image quality. Three-dimensional data sets can therefore be rapidly acquired, opening the possibility of comprehensive screening. Recent work has demonstrated the use of SD-OCT in ophthalmic applications at increased speeds [8, 11, 12]; A-line acquisition times of 64  $\mu\text{s}$  [12] and 40  $\mu\text{s}$  [13] were reported. Since the duty cycle of these systems was limited to 5% or less by data transfer, however, the effective image acquisition speed was limited to 768 [12] and 640 [13] A-lines per second. Our group has previously published results demonstrating acquisition and data transfer speeds of 34.1  $\mu\text{s}/\text{Aline}$  [8], resulting in an effective speed of 29,000 A-lines per second for a single image comprising 1000 A-lines.

In this paper we report video rate SD-OCT ophthalmic imaging with a duty cycle of 98% using a high speed line scan camera with simultaneous data acquisition and CameraLink™ data transfer capabilities. Charge transfer from photodiode area to on-chip storage area took 700 ns, constituting 2% of a line acquisition time of 34.1 μsec (Atmel TH7814A Linear CCD). The noise characteristics and the depth dependence of the sensitivity were characterized. A sustained acquisition rate of 29 fps at 1000 A-lines per frame and real-time display rate of 10 fps were realized. Three-dimensional reconstructions of the retina were created from the data collected. To our knowledge this is the first video-rate SD-OCT system presented and the fastest SD-OCT system reported.

## 2. Method

SD-OCT is based on spectral interferometry, where recombined light from reference and sample arms is spectrally separated, detected and converted into a depth profile. The detected interference signal at the spectrometer may be expressed as [3]

$$I(k) = I_r(k) + 2\sqrt{I_s(k)I_r(k)} \sum_n \alpha_n \cos(k z_n) + I_s(k) \quad (1)$$

where  $I_r(k)$  and  $I_s(k)$  are the wavelength-dependent intensities reflected from reference and sample arms, respectively, and  $k$  is the wavenumber. The second term on the right hand side of Eq. (1) represents the interference between light returning from reference and sample arms.  $\alpha_n$  is the square root of the sample reflectivity at depth  $z_n$ . Depth information is retrieved by performing an inverse Fourier transform of Eq. (1), yielding the following convolution [3],

$$\left| FT^{-1}[I(k)] \right|^2 = \Gamma^2(z) \otimes \left\{ \delta(0) + \sum_n \alpha_n^2 \delta(z - z_n) + \sum_n \alpha_n^2 \delta(z + z_n) + O\left[ I_s^2 / I_r^2 \right] \right\}, \quad (2)$$

with  $\Gamma(z)$  representing the envelope of the coherence function. The first term in the braces on the right hand side describes the autocorrelation signal from the reference arm and has magnitude unity. The second and third terms are due to interference between light returning from reference and sample arms and form two images, where each has magnitude on the order of  $I_s / I_r$ . These two terms provide mirror images, where one is retained. The final term, with magnitude on the order of  $I_s^2 / I_r^2$ , describes autocorrelation noise due to interference within the sample arm.  $I_s$  and  $I_r$  represent the total intensity reflected from sample and reference arms, respectively. Equation (2) indicates that the relative contribution of sample autocorrelation noise can be reduced by increasing the reference arm power with respect to the signal. Decreasing the detector integration time permits an increase in the reference arm power without saturating the detector, decreasing the ratio  $I_s^2 / I_r^2$  and consequently reducing the contribution of autocorrelation noise in ultra-high-speed SD-OCT.

In the shot noise limit, the signal to noise ratio (SNR) in the spectral domain system has been shown to be [6]:

$$SNR_{SD} = \frac{\eta P_{sample} \tau_i}{E_v}, \quad (3)$$

where  $\eta$  is the spectrometer efficiency,  $P_{sample}$  is the sample arm power returning to the detection arm,  $\tau_i$  is the detector integration time and  $E_v$  is the photon energy. Unlike the SNR in the time domain, Eq. (3) demonstrates that in the shot noise limit,  $SNR_{SD}$  is independent of the spectral width of the source. This implies that the axial resolution can be increased at no penalty to the SNR, provided that the full spectral width of the source can be imaged onto an array detector.

### 2.1 Ultra-high-speed spectrometer

The high-speed spectrometer of our SD-OCT system was described previously [8, 14] and is shown schematically in Fig. 1. Briefly, the fiber-based interferometer was illuminated using a superluminescent diode with a central wavelength of 840 nm and FWHM bandwidth of 50 nm, resulting in a measured axial resolution of 8.3  $\mu\text{m}$  in air based on the FWHM of the coherence envelope and, assuming a refractive index of 1.38 for the retina, 6  $\mu\text{m}$  in the eye. The lateral resolution as constrained by the focusing optics of the eye itself was approximated to be 30  $\mu\text{m}$  [15]. Telecentric imaging of the retina was controlled by a pair of scanning galvanometers in the slit-lamp [14], allowing the beam to be swept across the retina over a user-defined region of interest. Light from the source was directed to the reference and sample arms using an 80/20 splitter with the larger fraction directed to the reference arm. The reference mirror was kept stationary throughout the experiments. Reference arm light was attenuated using a variable neutral density filter before returning to the detection arm, such that the maximum intensity on the detector reached approximately 90% of the camera's saturation value of 4.6 nW/pixel. Polarization controllers were used to maximize the interference between sample and reference light at the detector. The remaining 10% of the dynamic range of the 10-bit camera ( $\sim 100$  levels) was available to capture the modulation of the spectrum. In SD-OCT the reflectivity in  $z$ -space is given by the square of the Fourier component in  $k$ -space (Eq. (2)). The dynamic range of the Fourier component is given by the modulation depth of the spectrum ( $\sim 100$ ) multiplied with the number of illuminated pixels of the camera ( $\sim 1000$ ), resulting in a maximum dynamic range in  $z$ -space of  $\sim 100$  dB. The presence of multiple reflecting structures reduces the effective dynamic range, as does the presence of (shot) noise on the spectrum. Less than 600  $\mu\text{W}$  of power was used to illuminate the undilated eye of a healthy human volunteer, in compliance with ANSI standards [10]. The volunteer's head was stabilized using a chin and head rest on the slit lamp to minimize movement.

Light returning from reference and sample arms was recombined in a detection arm consisting of a 60 mm focal length achromatic collimating lens, a 1200 lines/mm transmission grating (Wasatch Photonics) set at Littrow's angle, and a 100 mm focal length air-spaced imaging lens. The focused light projected onto a CCD linescan camera (Basler Vision Technologies, Germany) consisting of 2048 pixels, each 10  $\mu\text{m}$  x 10  $\mu\text{m}$  in size. The designed spectral resolution of the system was 0.075 nm, corresponding to an axial scan range of 2.35 mm in air [3]. The spectrometer efficiency  $\eta$  was 28% [8].

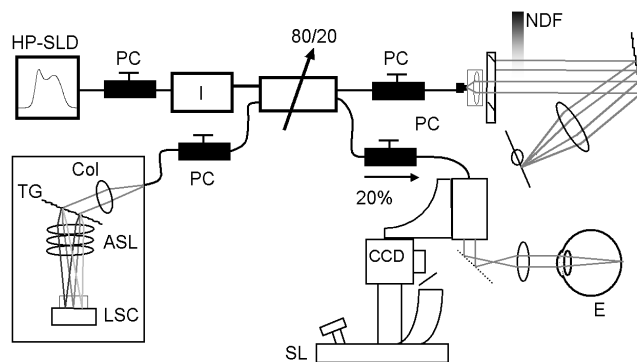


Fig. 1. Spectral-domain optical coherence tomography setup. The components of the system are: high-powered superluminescent diode source (HP-SLD), polarization controllers (PC), slit-lamp (SL), neutral density filter (NDF), collimator (Col), transmission grating (TG), air-spaced focusing lens (ASL), linescan camera (LSC), eye (E).

Data was acquired at a rate of 29.3 kHz, with each image consisting of 1000 consecutive spectra, thus allowing the capture of 29 fps. The central 1024 points of each spectrum, corresponding to a spectral range of 74 nm (798-872 nm), were downloaded via CameraLink<sup>TM</sup> and a high-speed image acquisition board (PCI 1428, National Instruments) to

the computer host memory (Dual P4 2.4 GHz, 1 GB RAM) with a resolution of 10 bits per pixel. Elimination of the peripheral 1024 points facilitated a reduction of the data stream from 120 MB/s to 60 MB/s, while simultaneously reducing the read-out noise contribution.

### 2.2 Video-rate acquisition and real-time display

Data acquisition software was designed in a similar fashion to that presented by Park *et al* [16] to ensure saving of all captured frames onto a hard disk. The program consists of a main control thread running an acquisition thread, which collected data continuously from the camera and deposited it onto the acquisition computer. Data was downloaded in real-time allowing for continuous data acquisition into buffers, where each buffer downloaded from the camera corresponded to one image frame (34.1 ms). When each image was acquired by the camera, the image buffer was transferred to a dynamically linked memory allocation. Image buffers were held in memory until saved by a separate thread. The FFT thread ran independently, grabbing the last acquired frame and processing it for display. Data was interpolated so that the points of the spectra were evenly distributed in  $k$ -space before Fourier transformation [11]. Due to the heavy computational load, the FFT thread processed and displayed 33% of the acquired frames, resulting in a display update rate of 10 fps. No additional image processing was performed on the real-time displayed images. Since the individual computing threads were independent, however, FFT processing did not interfere with the continuous archiving of data to hard disk at a rate of 29 fps.

### 2.3 Post processing

After acquisition, the raw data was filtered in order to remove fixed-pattern noise. For each image, two background spectra were generated: one by averaging all spectra from that image and the second by subsequently low-pass filtering this averaged spectrum to represent a smooth source spectrum. Each individual spectrum was then divided by the averaged background spectrum and then multiplied by the smoothed spectrum. This procedure removes all fixed-pattern noise in the image. Mapping errors due to linear interpolation appeared at greater depths as an increased background signal, or shoulders around the peaks [7, 17]. This error was corrected by using a zero-filling technique [17] to quadruple the number of points in the spectrum. This correction included Fourier transformation, zero padding to increase the data array length 4-fold, and inverse Fourier transformation back to the spectral domain but with 4 times as many points in the data array compared to the original. This spectrum was then linearly interpolated in  $k$ -space [11] and Fourier transformed into  $z$ -space to recover the depth profile, free of shoulders at longer depths. The post processing was performed in Matlab and took 19 seconds per image. The images were compiled into the movies presented below.

## 3. Results

### 3.1 Noise characterization of the SD-OCT system

The different noise components present in the system were measured and analyzed to demonstrate that performance was shot-noise-limited. The read-out and shot noise at a 29.3 kHz read-out rate are shown in Fig. 2.

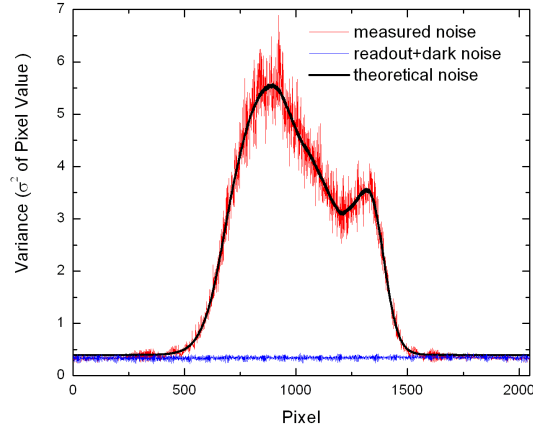


Fig. 2. Noise components in the detector. The shot noise level was determined with illumination of the reference arm only, and was used to determine the A/D resolution of the detector. The theoretical shot noise curve was fit using Eq. (4) to the measured noise, giving a  $\Delta e$  of 173 electrons and a corresponding well depth of 177,000 electrons.

The noise was determined by calculating the variance at each camera pixel for 1000 consecutive spectra. Dark noise measurements were taken with the source light off. Only light returning from the reference arm was used to measure the shot noise in the system. The shot noise expressed in number of electrons is  $(I_{PV}(\lambda)\Delta e)^{1/2}$ , where  $I_{PV}(\lambda)$  is the pixel value corresponding to the intensity at each CCD element, with values ranging from 0 to 1024 (10-bits) and  $\Delta e$  is the analogue-to-digital conversion resolution, which corresponds to the number of electrons required for an incremental increase of 1 pixel value. Thus, the variance as measured in pixel values is defined as:

$$\sigma^2(\lambda) = I_{PV}(\lambda)/\Delta e + \sigma_{r+d}^2. \quad (4)$$

The first term on the right hand side of Eq. (4) is the shot noise contribution and the second term is the read-out contribution to the total noise. The CCD well depth was determined by fitting the theoretical expression for shot noise to the measured shot noise, using  $\Delta e$  as the fitting parameter and limiting the fit to the central 700 pixels. From this measurement,  $\Delta e$  was calculated to be 173 electrons. Assuming that the maximum pixel value corresponds to the full well depth, a well depth of 177,000 electrons was calculated, in agreement with our previously published result [8]. Shot noise dominated read-out and dark noise when the intensity reached 6% of the saturation value. Relative intensity noise (RIN) is never dominant in this setup, since the maximum power per pixel (4.6 nW) at a 34.1  $\mu$ s integration time does not meet the criteria for RIN dominated noise [8].

In SD-OCT, signal sensitivity is strongly dependent on depth within an image. To characterize our system sensitivity as a function of ranging depth, 1000 A-lines were acquired at an acquisition speed of 34.1  $\mu$ s/A-line for 9 different positions of a weak reflector in the sample arm. The reflected sample arm power was 1.18 nW for all reflector positions. The noise floor without zero-padding decayed by 5 dB between a depth of 500  $\mu$ m and 2 mm, and the peak signal dropped by 21.7 dB over the first 2 mm. Due to fixed-pattern noise, the true noise floor could not be determined between 0 and 500  $\mu$ m. The removal of fixed-pattern noise as described in section 2.3 was not applied to this sensitivity measurement. After zero-filling to correct mapping errors as described in section 2.3, a 16.7 dB loss in peak signal was noted across the first 2 mm, whereas the noise level dropped by only 0.4 dB between 500  $\mu$ m (35.1 dB) and 2 mm (34.7 dB) (Fig. 3). The zero-filling method produced a nearly constant noise level and improved the signal by more than 5 dB at the greatest depths in the

scan. Although zero-filling did not change the local SNR, this method eliminated the shoulders that are present at larger scan depths [7]. The decay in both the signal and the noise level across the entire scan length of 2.4 mm have been theorized to amount to 4 dB as a result of the finite pixel width [5]. As demonstrated by the experimental data, the noise level decayed by less than 4 dB over the entire scan length, which we attribute to the statistical independence of the shot noise between neighboring pixels of the array. Thus, the finite pixel width does not introduce a decay of the noise level.

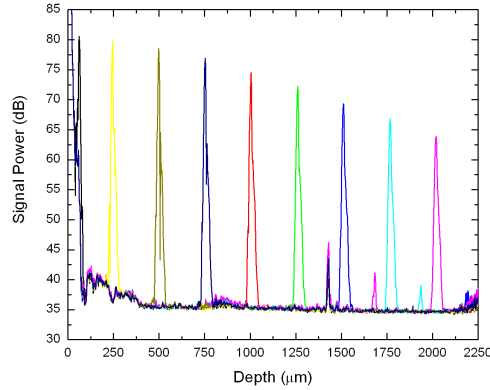


Fig. 3. The depth dependent loss in signal sensitivity from a weak reflector. The signal decayed 16.7 dB between 0 and 2 mm. The peaks at 1.4 mm, 1.6 mm, and 1.85 mm are fixed pattern noise .

The finite spectrometer resolution introduces a sensitivity decay [18] similar to that introduced by the finite pixel size [5]. Convolution of the finite pixel size with the Gaussian spectral resolution yields the following expression for the sensitivity reduction,  $R$ , as a function of imaging depth,  $z$  [18],

$$R(z) = \frac{\sin^2(\pi z/2d)}{(\pi z/2d)^2} \exp\left[-\frac{\pi^2 \omega^2}{8 \ln 2} \left(\frac{z}{d}\right)^2\right] \quad (5)$$

where  $d$  is the maximum scan depth, and  $\omega$  is the ratio of the spectral resolution to the sampling interval. Equation (5) was fit to the signal decay data presented in Fig. 3 with  $\omega$  as a free parameter, and the result shown in Fig. 4. Due to its proximity to the autocorrelation peak, the first data point was not included in the fit. The value for  $\omega$  obtained from the fit was 1.85, demonstrating that the working spectral resolution was 0.139 nm.

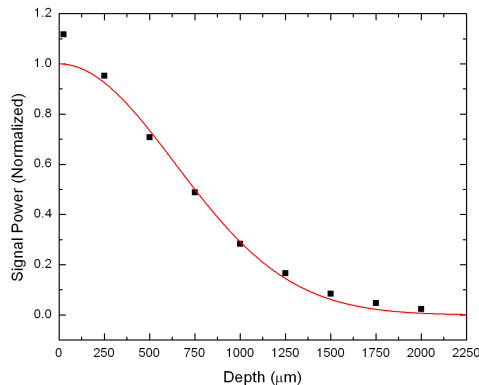


Fig. 4. Decay of sensitivity across the measurement range. Symbols: Peak intensities of data presented in Fig 3. Solid line: Fit of Eq. (5) to the data points.

The SNR was determined by the ratio of the peak at 250  $\mu\text{m}$  (79.8 dB) and the noise level. Due to the fixed-pattern noise at 250  $\mu\text{m}$ , the noise level was determined to be 35.2 dB by extrapolation of the linear region between 0.5 and 2 mm. The resulting SNR of 44.6 dB for 1.18 nW returning to the detection arm was 2.2 dB below the theoretical value given by Eq. (3) of 46.8 dB, for an integration time of 34.1  $\mu\text{sec}$ , a central wavelength of 840 nm and a spectrometer efficiency of 28%. With 600  $\mu\text{W}$  of power incident on an ideal reflector in the sample arm, the measured power returning to the detection arm was 284  $\mu\text{W}$ . The sum of the SNR at 1.18 nW (44.6 dB) and the 10 Log ratio of maximum (284  $\mu\text{W}$ ) over measured (1.18 nW) power (53.8 dB) gives a sensitivity of 98.4 dB.

### 3.2 Video-rate images

A 10.7 second scan of the fovea yielded the movie sequence shown in Fig. 5. A sequence of 310 images (3.2 mm wide by 1.0 mm deep) was acquired across the macula, tracing out an area 2.56 mm long. Due to publication constraints, the image size was reduced to 512 x 164 pixels from 1000 x 320 pixels, and the images were cropped to remove the autocorrelation peak at zero and the deeper, unused portion of the image. The movie sequence was grayscale coded over 46 dB where the minimum was set at 32 dB, 3 dB below the noise floor as determined from Fig. 3 and the maximum was taken as the absolute maximum intensity in the movie sequence. The layers of the macula are clearly identifiable and correlate with previously published OCT images of the fovea [9].

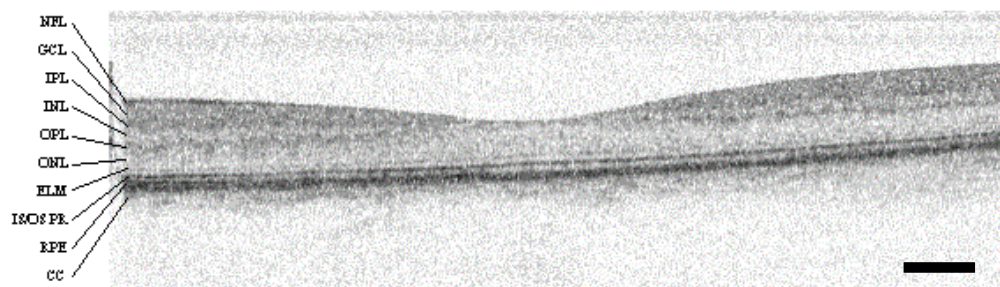


Fig. 5. (2.0 MB) Movie of the fovea acquired at 29 fps with 1000 A-lines/frame. The movie sweeps over a length of 2.56 mm, with each frame consisting of an image 3.2 mm wide by 1 mm deep. Frame # 154 of 310 is shown above. The individual layers of the fovea are distinguishable and labeled: Nerve fiber layer (NFL), ganglion cell layer (GCL), inner plexiform layer (IPL), inner nuclear layer (INL) outer plexiform layer (OPL), outer nuclear layer (ONL), external limiting membrane (ELM), inner and outer segment of photoreceptors (IS/OS PR), outer nuclear layer (ONL), the retinal pigment epithelium (RPE), and choriocapilaris (CC). The scale bar represents 250  $\mu\text{m}$ . (8.33 MB version)

The region around the optic nerve was also imaged. Figure 6 shows a representative frame from a 13.1 second movie sequence centered on the optic nerve head. The data set consisted of 380 images, each 6.4 mm wide by 1.7 mm deep and covered a region 5.12 mm in length. The images are coded over 44 dB determined in the same manner as the dynamic range of Fig. 5. As the scan moves through the optic nerve head, several blood vessels are seen. Shadows associated with blood vessels are easily seen in the movie, tracking with the vessels entering the optic nerve head [19].



Fig. 6. (2.0 MB) Movie of a region around the optic nerve head, acquired in 13.1 seconds at a rate of 29 fps with 1000 A-lines/frame. Each image is 6.4 mm wide x 1.7 mm deep. The sequence sweeps over a region 5.12 mm long, with frame # 134 of 380 shown above. The retinal vasculature is seen both in the layers of the retina and converging in the optic nerve head itself. The scale bar represents 500  $\mu\text{m}$ . (8.89 MB version)

The vascular network of the retina can be visualized further by generating a 3-dimensional reconstruction of the optic nerve head. The data from Fig. 6 were compiled into the 3-D volume shown in Fig. 7(a), cut *en-face* and compared to a fundus photograph of the same region seen in Fig. 7(b). The two most prominent layers are the nerve fiber layer (NFL) and the retinal pigment epithelium (RPE), identifiable as the dark concentric features in Fig. 7(a). Branches of the vascular tree are also evident and correlate with the pattern of the vasculature observed using standard imaging techniques. The same bifurcation is seen within the dashed box in each image of Fig. 7.

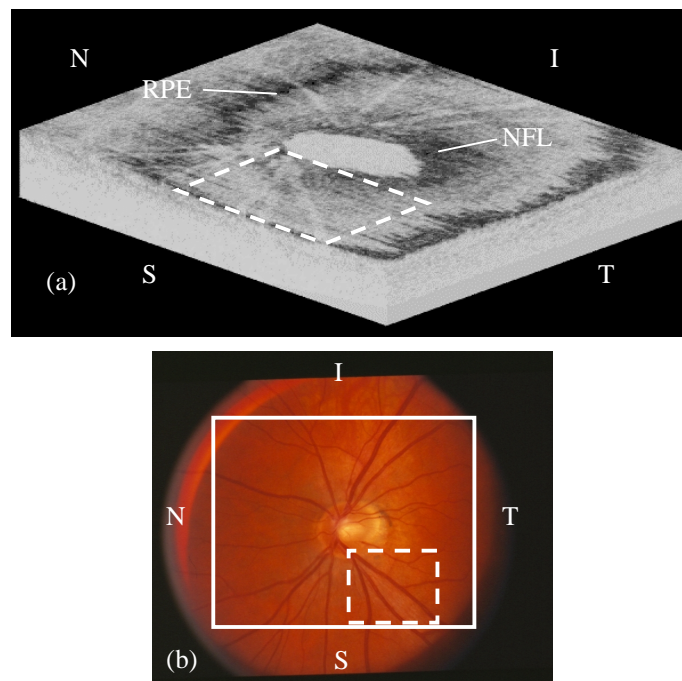


Fig. 7. (a) (2.5 MB) 3-dimensional reconstruction of the retina from the images composing Fig. 6. The vascular network is visible as shadows in the retinal layers as seen in the *en-face* 3-D reconstruction. The RPE and NFL are the two prominent dark layers that appear in the volume. (b) Fundus photograph of the same retina used for OCT imaging. The bifurcation marked with dashed box corresponds to the bifurcation seen in the 3-D reconstruction. Orientation: S = superior, I = inferior, N = nasal, T = temporal.

#### **4. Conclusions**

We have demonstrated sustained video-rate acquisition at 29 fps and real-time image display at 10 fps using spectral-domain optical coherence tomography, with integration times of 34.1  $\mu$ sec and an axial resolution of 6  $\mu$ m in the eye. The system acquired and displayed data continuously, at a 98% duty cycle. The detection sensitivity of the system was analyzed and shown to be limited by shot noise. In addition, we showed that the decrease in sensitivity across the scan depth was well described by a convolution of the pixel size with the spectral resolution. The unprecedented ultra-high-speed of this system eliminates motion artifacts and the need to re-align A-lines, enabling accurate 3-D mapping of the retina and optic nerve. This capability is essential to the diagnosis and monitoring of glaucoma, the second leading cause of blindness in the world. The high resolution of this system, which enables better delineation of the retinal layers, will also improve the clinical utility of OCT in the understanding, diagnosis, and treatment of numerous ophthalmic diseases.

#### **Acknowledgments**

This research was supported in part by research grants from the National Institutes of Health (1R24 EY12877, R01 RR019768), Department of Defense (F4 9620-021-1-0014), the Whitaker Foundation (26083), Center for Integration of Medicine and Innovative Technology (CIMIT), and a gift from Dr. and Mrs. J.S. Chen to the Optical Diagnostics Program at the Wellman Center for Photomedicine.